Research Square

Preprints are preliminary reports that have not undergone peer review.
They should not be considered conclusive, used to inform clinical practice,
or referenced by the media as validated information.

T2WI-based intratumoral habitat and peritumoral radiomics to predict lymph node metastasis in cervical cancer: a multicenter study with biological validation

Yanhong Lyu
Air Force Medical University
Yang Wang
Air Force Medical University
Haixia Liu
Shandong Provincial Hospital
Shujuan Liu
Air Force Medical University
Yunge Gao
Xi'an People's Hospital
Jie Luo
Xi'an People's Hospital
Miao Zhang
Shandong Provincial Hospital
Jia Li
Air Force Medical University
Xue Han
Shengjing Hospital of China Medical University
Jing Ren
Air Force Medical University
Biliang Chen
fkcbl123456@163.com

Air Force Medical University

Research Article

Keywords: Cervical cancer, Lymph node metastasis, Habitat radiomics, Nomograms, Magnetic Resonance Imaging

Posted Date: November 6th, 2026

DOI: https://doi.org/10.21203/rs.3.rs-11336411/v1

License: This work is licensed under a Creative Commons Attribution 4.0 International License. Read Full License

Additional Declarations: No competing interests reported.

Abstract

Background

To develop and validate a T2WI-based nomogram integrating intratumoral habitat imaging, peritumoral radiomics, and clinical features for preoperative prediction of lymph node metastasis (LNM) in cervical cancer (CC), and to verify the biological plausibility of imaging habitats using an animal model.

Methods

This multicenter study included 766 CC patients (IB1-IIA2 and IIIC) from four centers, divided into training (n = 219), internal validation (n = 94), and two external test cohorts (n = 269, n = 184) between 2020 and 2024. Habitat imaging and peritumoral features were extracted, followed by machine-learning model construction, evaluation, and SHAP interpretability. For biological validation, 12 nude mice bearing HeLa, SiHa, and U14 tumors underwent 9.4T MRI; imaging-pathology spatial registration was performed using 3D-printed molds, and habitat consistency was quantified by the Adjusted Rand Index (ARI) and intraclass correlation coefficient for area (ICC(area)).

Results

Clinical stage and tumor diameter ≥ 4 cm were independent risk factors for LNM (both $P < 0.05$). The combined model yielded AUCs of 0.933 (training), 0.898 (internal validation), and 0.858–0.863 (external tests). A nomogram with a Youden-derived cutoff of 0.32 demonstrated consistent sensitivity (0.818–0.913) and specificity (0.732–0.877) across cohorts, with good calibration (Hosmer-Lemeshow $P = 0.183–0.561$). Animal experiments revealed moderate spatial correspondence (ARI: 0.4–0.6) and high proportional consistency (ICC (area): 0.8–1.0) between imaging and pathological habitats.

Conclusions

This T2WI-based intratumoral habitat and peritumoral radiomics model provides accurate, economical preoperative LNM prediction for CC to guide personalized radiotherapy or surgery, with biological validity confirmed by animal experiments.

Trial registration

ChiCTR2400081731, Registered 11 March 2024, https//www.chictr.org.cn/showproj.html?proj=203940

Background

Cervical cancer (CC) is a prevalent gynecological malignancy, ranking fourth among women worldwide[1]. Accurate preoperative identification of lymph node metastasis (LNM) is critical as it dictates whether patients receive radical surgery or definitive chemoradiotherapy[2, 3]. However, standard MRI criteria based on nodal size and morphology have inferior sensitivity (41.2%-61.7%)[4, 5], particularly for normal-sized metastatic lymph nodes, resulting in false-negative evaluations and improper treatment planning[6]. Although radiomics improves prediction, most models overlook intratumoral heterogeneity, a key biological trait of tumor aggressiveness[7–9].

By dividing tumors into subregions with unique biological activities, habitat imaging, an extension of radiomics, addresses this constraint and captures spatial heterogeneity within the tumor microenvironment[10, 11]. Studies of the nervous system, breast, liver, and other malignancies have shown a much higher accuracy than traditional radiomics, enabling a more nuanced perspective for tumor diagnosis and treatment[12, 13]. However, its application in LNM of CC remains limited. Therefore, we developed a T2WI-based model integrating intratumoral habitat, peritumoral radiomics, and clinical features to predict preoperative LNM. A secondary aim was to validate the biological plausibility of these habitats via MRI-to-histology registration in animal models (Fig. 1).

Methods

Study Design and Patient Selection

This multicenter retrospective study screened 955 patients with stage IB1–IIA2 and IIIC CC (FIGO 2018) from four hospitals (2020–2024). The study was approved by the institutional ethics committees of center (Approval Number: KY20232107-F-1) and registered in the Chinese Clinical Trial Registry (ChiCTR2400081731). Given the study's retrospective design and the anonymity of the patient data, informed consent waivers were obtained. This study followed the guidelines of the Declaration of Helsinki and local regulations.

The inclusion criteria were: (i) histopathologically confirmed squamous cell carcinoma or adenocarcinoma of the cervix, (ii) radical hysterectomy and pelvic lymphadenectomy with postoperative pathological confirmation of lymph node status, and (iii) completion of pelvic MRI within two weeks before surgery. Exclusion criteria were: (i) neoadjuvant chemotherapy or chemoradiotherapy, (ii) lesions < 0.5 cm on preoperative MRI, and (iii) incomplete imaging or clinical data. Ultimately, 766 eligible patients were included (center 1, n = 266; center 2, n = 47; center 3, n = 269; and center 4, n = 184). All clinical and imaging data of the patients were obtained from the electronic medical record system. LNM was confirmed by two blinded pathologists, with consensus reached for any discrepancies. centers 1 and 2 were randomly assigned to training (70%) and internal validation (30%), whereas centers 3 and 4 were independent external test cohorts for generalizability. The patient selection workflow is shown in Supplementary eFigure 1.

MRI Preprocessing and ROI Delineation

All patients underwent pelvic MRI with T2WI (parameters in Supplementary Materials eMethods 1). To harmonize multi-center data and enhance model generalizability, all images underwent standardized preprocessing: isotropic resampling to 1.0 mm^3 voxel spacing, N4 bias field correction to address intensity inhomogeneity, and Z-score intensity normalization to eliminate inter-scan grayscale fluctuations. Region of interest (ROI) delineation was performed independently by two radiologists who were blinded to clinical and pathological data. Inter-observer agreement was assessed using the intraclass correlation coefficient (ICC). Features with ICC < 0.8 were excluded; those with ICC ≥ 0.8 were retained for subsequent analysis.

Habitat and Peritumoral Region Analysis

Peritumoral regions were generated by radial expansion of the ROI at 1, 3, and 5 mm using the OnekeyAI platform, with manual correction of abnormal expansions. The optimal peritumoral distance was determined by model performance comparison (supplementary eFigure 2).

Habitat imaging was used to quantify the intratumoral heterogeneity. For each voxel within the tumor volume, 19 local radiomic features—including first-order statistics and texture parameters—were extracted via a 3D sliding window approach (window size: 5×5×5 voxels; step size: 1 voxel) (supplementary eMethods 2). These voxel-wise feature vectors were then clustered using the K-means algorithm[14] to segment the tumor into biologically distinct subregions. To ensure reproducibility, the algorithm was initialized with a fixed random seed, run with 100 random initializations to avoid local optima, and applied using a locked, standardized pipeline on the OnekeyAI platform (version 3.5.12, Python 3.7.12). The optimal cluster number was determined by evaluating the Calinski-Harabasz (CH) index, Davies-Bouldin (DB) index, and Silhouette Coefficient (SC) across k = 3 to 10 (supplementary eMethods 2). The resulting habitat maps provided a refined representation of intratumoral heterogeneity (supplementary eFigure 2).

Feature Extraction and Selection

Feature Extraction and Selection
Radiomic features were independently extracted from the intratumoral region, each peritumoral expansion (1, 3, and 5 mm), and each habitat subregion using PyRadiomics (v3.0.1) in compliance with IBSI standards. For each region, 1,547 features were extracted, comprising 14 shape descriptors, 360 first-order statistics, and 1,173 texture features derived from gray-level co-occurrence matrix (GLCM), gray-level run-length matrix (GLRLM), gray-level size zone matrix (GLSZM), and neighboring gray-tone difference matrix (NGTDM) matrices. For the Habitat Signature, features from the three subregions were fused by early concatenation, yielding 4,641 habitat-derived features. Missing feature values in habitat subregions were imputed via KNN (K = 5) prior to fusion.

All feature selection steps—univariate filtering ($P < 0.05$), Pearson correlation ($|r| > 0.9$), the Minimum Redundancy Maximum Relevance (mRMR) (top 32), and Least Absolute Shrinkage and Selection Operator (LASSO) logistic regression with 10-fold cross-validation—were performed exclusively on the training cohort and locked before validation. The optimal regularization parameter λ for each signature was selected using the 1-SE rule, and Rad-scores were calculated for each signature as linear combinations of the retained features weighted by their respective LASSO coefficients (supplementary eMethods 3).

Model Construction

Five machine learning algorithms—Support Vector Machine (SVM), Random Forest (RF), Extra Trees, XGBoost, and LightGBM—were independently applied to each signature (Intratumoral, Peri1mm, Peri3mm, Peri5mm, and Habitat) using features pre-selected by LASSO. Hyperparameters for each algorithm were tuned via grid search with 5-fold cross-validation within the training cohort. The optimal algorithm for each signature was selected based on the highest cross-validated area under the curve (AUC). For clinical utility, a nomogram integrating independent clinical predictors with the best-performing signature was developed using multivariate logistic regression in the training cohort (supplementary eMethods 4). The optimal probability cutoff was determined by maximizing the Youden index in the training cohort and applied without recalibration to all validation cohorts.

Animal Experiment for Biological Validation

All animal procedures were approved by the Institutional Animal Ethics Committee (Approval Number: 20250031). Female BALB/c nude mice (4–6 weeks old, 18–20 g) were purchased from the Experimental Animal Center of the University (Xi'an, China) and housed under specific pathogen-free conditions with a 12-h light/dark cycle, with free access to standard chow and water. All animals were experimentally naive and were acclimatized for one week before tumor inoculation. Three cell lines—human HeLa and SiHa, and murine U14—were cultured and validated via short tandem repeat profiling. All cells were cultured and subcutaneously inoculated into nude mice (n = 6 per cell line) to establish subcutaneous transplantation tumor models (Supplementary eMethods 5).

When the tumor volume reached 1000–1500 mm^3, T2-weighted imaging was acquired on a 9.4T Bruker BioSpec 94/20 USR small-animal MRI scanner under anesthesia with 2–3% isoflurane in oxygen (induction 3–4%, maintenance 1.5–2%), with respiratory rate monitored throughout. After scanning, animals were euthanized by an intraperitoneal overdose of pentobarbital sodium (150 mg/kg) following deep anesthesia, and death was confirmed by the absence of a heartbeat and corneal reflex before tumor excision. This method is consistent with the American Veterinary Medical Association (AVMA) Guidelines for the Euthanasia of Animals. Tumors were then excised, fixed, and sectioned at 2 mm intervals into 5–8 tissue blocks per tumor using customized 3D-printed molds. The molds, designed with parallel guiding slits and positioning pins, ensured spatial orientation consistent with MRI slices during sectioning (eMethods 5, eFigure 3). H&E-stained sections were registered to matching MRI slices using the “contour-plus-centroid” method (eMethods 5). Sections with Dice coefficient > 0.8 and IoU > 0.7 were selected for comparative analysis. Imaging habitats were segmented via K-means clustering, while pathological habitats were clustered using hierarchical clustering to reflect histologic features (eMethods 5). To evaluate the consistency between imaging and

pathological habitat analyses, we employed the Adjusted Rand Index (ARI)[15] to quantify spatial correspondence and the Intraclass Correlation Coefficient of Area (ICC(area)) [16] to assess compositional agreement in subregion proportions.

Statistical Analysis

Continuous variables were compared using t-test or Mann-Whitney U test, and categorical variables using χ^2 test. Univariate and multivariate logistic regression identified clinical factors for LNM. Model performance was assessed by AUC, accuracy, sensitivity, specificity, PPV, and NPV with 95% CIs from 1000 bootstrap resamples. The optimal cutoff was derived from the Youden index in the training cohort. Calibration was evaluated using the Hosmer-Lemeshow (HL) test with calibration curves. DeLong test compared AUCs. Decision curve analysis (DCA) assessed clinical utility. SHAP was used for model interpretability. Python 3.7.12 (Statsmodels v0.13.2, Scikit-learn v1.0.2) was used for statistical analyses and modeling; PyRadiomics v3.0.1 for feature extraction; MATLAB R2024a for ARI and ICC (area) calculations. Statistical significance was set at $P < 0.05$.

Results

Clinical Characteristics

A total of 766 eligible patients who underwent radical surgery were selected from an original cohort of 955 patients. Patients were divided into four groups: training (n = 219), internal validation (n = 94), and two separate external test cohorts (n1 = 269 and n2 = 184). The clinical characteristics of each cohort at the baseline are summarized in Table 1. Clinical stage and tumor diameter of the LNM-negative and LNM-positive groups were significantly different across all cohorts. However, no significant differences were observed in the other baseline variables.

Table 1
Baseline characteristic of our cohorts.

Variables	Train (n = 219)		*P* value	Val (n = 94)		*P* value	External test sets1 (n = 269)		*P* value	External test sets2 (n = 184)		*P* va
	LNM(-)n = 163	LNM(+)n = 56		LNM(-)n = 71	LNM(+)n = 23		LNM(-)n = 233	LNM(+)n = 36		LNM(-)n = 162	LNM(+)n = 22	
Age(year)	51.8 ± 12.2	49.2 ± 12.0	0.169	53.4 ± 11.5	48.6 ± 11.3	0.086	52.0 ± 11.0	50.2 ± 11.3	0.356	48.6 ± 11.2	46.3 ± 10.0	0.3
BMI(kg/m2)	23.1 ± 3.1	23.3 ± 2.9	0.663	22.6 ± 3.2	22.8 ± 2.8	0.869	23.6 ± 3.3	23.3 ± 2.9	0.517	24.5 ± 3.6	23.6 ± 3.7	0.2
PAR			0.518			1			1			0.6
<3.74	23 (14.1)	6 (10.7)		8 (11.3)	3 (13.0)		12 (5.2)	2 (5.6)		9 (5.6)	0 (0.0)	
≥ 3.74	140 (85.9)	50 (89.3)		63 (88.7)	20 (87.0)		221 (94.8)	34 (94.4)		153 (94.4)	22 (100.0)	
PLR			0.767			0.684			1			1
<93.1	18 (11.0)	7 (12.5)		6 (8.5)	3 (13.0)		30 (12.9)	4 (11.1)		10 (6.2)	1 (4.5)	
≥ 93.1	145 (89.0)	49 (87.5)		65 (91.5)	20 (87.0)		203 (87.1)	32 (88.9)		152 (93.8)	21 (95.5)	
SII			0.529			0.97			1			0.2
<717.9	106 (65.0)	39 (69.6)		46 (64.8)	15 (65.2)		202 (86.7)	31 (86.1)		109 (67.3)	12 (54.5)	
≥ 717.9	57 (35.0)	17 (30.4)		25 (35.2)	8 (34.8)		31 (13.3)	5 (13.9)		53 (32.7)	10 (45.5)	
STAGE			< 0.001			0.452			< 0.001			< 0.0
Stage I	91 (55.8)	21 (37.5)		41 (57.7)	11 (47.8)		167 (71.7)	17 (47.2)		116 (71.6)	5 (22.7)	
Stage II	59 (36.2)	20 (35.7)		23 (32.4)	11 (47.8)		50 (21.5)	4 (11.1)		39 (24.1)	8 (36.4)	
Stage III	13 (8.0)	15 (26.8)		7 (9.9)	1 (4.3)		16 (6.9)	15 (41.7)		7 (4.3)	9 (40.9)	
Diameter(cm)	3.1 ± 1.2	3.5 ± 1.2	0.031	2.8 ± 1.1	3.6 ± 1.1	0.003	2.6 ± 1.0	3.8 ± 1.4	< 0.001	3.0 ± 1.2	3.9 ± 1.2	0.0
HPV			0.268			0.374			0.269			0.6
16/18+	5 (3.1)	3 (5.4)		4 (5.6)	1 (4.3)		4 (1.7)	0 (0)		4 (2.5)	1 (4.5)	
other high risk type	138 (84.7)	50 (89.3)		61 (85.9)	22 (95.7)		189 (81.1)	26 (72.2)		146 (90.1)	20 (90.9)	
negative	20 (12.3)	3 (5.4)		6 (8.5)	0 (0.0)		40 (17.2)	10 (27.8)		12 (7.4)	1 (4.5)	
Pathological			0.413			0.581			0.614			0.4
SCC	141 (86.5)	47 (83.9)		59 (83.1)	17 (73.9)		185 (79.4)	27 (75)		133 (82.1)	20 (90.9)	
AC	15 (9.2)	4 (7.1)		4 (5.6)	2 (8.7)		36 (15.5)	8 (22.2)		22 (13.6)	1 (4.5)	
Others	7 (4.3)	5 (8.9)		8 (11.3)	4 (17.4)		12 (5.2)	1 (2.8)		7 (4.3)	1 (4.5)	

Abbreviates: BMI: body mass index; PAR：Platelet-to-Albumin Ratio, PLR：Platelet-to-Lymphocyte Ratio and SII：Systemic Immune-Inflammation Index;SCC：Squamous Cell Carcinoma；AC：adenocarcinoma；Others：adenosquamous carcinoma ；

Note

stage I : IB1-IB3 stage (FIGO 2018), stage II：IIA1-IIA2 stage (FIGO 2018),stage III：IIIC1r-IIIC2r (FIGO2018). PLR, PAR, and SII were classified using logistic regression knee point analysis.

Given that inflammatory composite markers have been reported as independent predictors of prognosis in CC[17], we incorporated the platelet-to-albumin ratio (PAR), platelet-to-lymphocyte ratio (PLR), and systemic immune-inflammation index (SII) into our analysis, in addition to conventional clinical indicators. Univariate and multivariate logistic regression analyses were performed to evaluate the associations between clinical variables and LNM. The results identified tumor diameter ≥ 4 cm (odds ratio [OR]: 2.70; 95% confidence interval [CI]: 1.74–4.19; $P < 0.001$) and clinical stage (OR: 1.65; 95% CI: 1.04–2.63; $P = 0.035$) as independent risk factors for LNM. However, none of the inflammatory markers showed a significant correlation with LNM. Detailed results of the univariate and multivariate analyses are presented in Table 2.

Table 2
Univariate and multivariate analysis of risk factors

Variable	Univariate analysis		Multivariate analysis	
	crude.OR (95%CI)	crude.*P* value	adj.OR (95%CI)	adj.*P* value
Age(year)				
<64	reference	1	reference	1
≥ 65	0.75 (0.40 ~ 1.43)	0.39	0.85 (0.43 ~ 1.68)	0.634
BMI(kg/m^2)				
<25.1	reference	1	reference	1
≥ 25.1	0.86 (0.56 ~ 1.3)	0.463	0.85 (0.54 ~ 1.33)	0.473
PAR				
<3.74	reference	1	reference	1
≥ 3.74	1.03 (0.52 ~ 2.03)	0.927	1.28 (0.61 ~ 2.69)	0.512
PLR				
<93.1	reference	1	reference	1
≥ 93.1	0.92 (0.51 ~ 1.67)	0.787	0.74 (0.38 ~ 1.43)	0.367
SII				
<717.9	reference	1	reference	1
≥ 717.9	1.15 (0.76 ~ 1.73)	0.502	0.85 (0.53 ~ 1.35)	0.486
STAGE				
Stage I	reference	1	reference	1
Stage II	1.93 (1.25 ~ 3)	0.003	1.65 (1.04 ~ 2.63)	0.035
Stage III	7.15 (4.27 ~ 11.97)	< 0.001	5.77 (3.35 ~ 9.94)	< 0.001
Diameter(cm)				
<4	reference	1	reference	1
≥ 4	3.48 (2.33 ~ 5.18)	< 0.001	2.7 (1.74 ~ 4.19)	< 0.001
HPV				
16/18+	reference	1	reference	1
other high risk type	0.75 (0.27 ~ 2.08)	0.582	0.8 (0.27 ~ 2.38)	0.685
negative	0.61 (0.19 ~ 1.92)	0.399	0.7 (0.20 ~ 2.40)	0.571
Pathological				
SCC	reference	1	reference	1
AC	0.91 (0.50 ~ 1.64)	0.752	1.03 (0.54 ~ 1.94)	0.935
Other	1.51 (0.74 ~ 3.07)	0.255	1.74 (0.82 ~ 3.71)	0.148

Abbreviates: BMI: body mass index; PAR：Platelet-to-Albumin Ratio, PLR：Platelet-to-Lymphocyte Ratio and SII：Systemic Immune-Inflammation Index;SCC：Squamous Cell Carcinoma；AC：adenocarcinoma；Others：adenosquamous carcinoma ；

Note:stage I: IB1-IB3 stage(FIGO 2018), stage II：IIA1-IIA2 stage(FIGO 2018), stage III：IIIC1r-IIIC2r(FIGO 2018). BMI, Age, PLR, PAR, and SII were classified using logistic regression knee point analysis.

Handcrafted Features

Evaluation of the CH, DB, and SC indices across k = 3 to 10 identified k = 3 as the optimal cluster number (Supplementary eFigure 4A–B). For each region, 1,547 radiomic features (14 shape, 360 first-order, 1,173 texture) were extracted. The Habitat Signature comprised 4,641 features after fusion across three subregions. LASSO regression selected features with non-zero coefficients for Rad-score calculation (Supplementary eFigures 4C and 5).

Habitat Signature Performance

In the internal validation cohort, the RF classifier achieved the highest area under curve (AUC) (0.896, 95% CI: 0.829–0.963), outperforming LightGBM (AUC = 0.880), Extra Trees (AUC = 0.889), XGBoost (AUC = 0.854), and SVM (AUC = 0.831). RF was therefore selected as the optimal classifier for the habitat signatures. Performance metrics for all algorithms across all cohorts are summarized in eTable 1, with corresponding ROC curves in eFigure 6.

Supplementary Materials Details A and B describe the radiomic and peritumoral feature extraction analyses, respectively. Details C explained the clinical model.

SHAP Value Analysis

SHAP analysis was applied to the RF-based Habitat Signature model to quantify the feature contributions to LNM prediction (Fig. 2). Among the top ten most influential features, H1 subregion attributes accounted for the largest number (5 of 10). However, when examining the directionality of predictions, H2-derived features consistently showed positive SHAP values driving LNM-positive classification, while H1 features exhibited negative SHAP values, indicating their role in excluding LNM. H3 features had consistently low SHAP values, suggesting minimal contribution. These opposing roles of H1 and H2 subregions highlight the value of habitat partitioning in capturing biologically distinct intratumoral populations with different metastatic propensities.

A: Distribution of SHAP values across habitat-derived features for all samples, highlighting their relative contribution to LNM prediction. B: The features are ranked according to their mean absolute SHAP values to identify the most influential predictors in the model. C: It provides patient-level interpretability through two representative cases: C1 illustrates a patient with LNM, where positive SHAP contributions from key features shift the prediction of metastasis, whereas C2 depicts a patient without LNM, in which negative SHAP contributions suppress the likelihood of metastasis.

Signature Comparison

The combined model achieved the highest AUCs across all cohorts: 0.933 (95% CI: 0.901–0.966) in training, 0.898 (95% CI: 0.833–0.963) in internal validation, 0.858 (95% CI: 0.796–0.921) in external test 1, and 0.863 (95% CI: 0.785–0.941) in external test 2, compared with the habitat-only model (AUCs: 0.914, 0.896, 0.822, and 0.829, respectively). However, DeLong tests showed that the improvement over the habitat-only model was not statistically significant in the internal validation (P = 0.830), external test 1 (P = 0.054), or external test 2 (P = 0.234) cohorts (eFigure 7). Among peritumoral models, Peri3mm consistently outperformed Peri1mm and Peri5mm, with AUCs of 0.745 (training), 0.714 (validation), 0.727 (external test 1), and 0.707 (external test 2), and was selected as the optimal peritumoral signature for integration into the combined model. The corresponding ROC curves for all models are displayed in Fig. 3A–D.These results indicate that the Habitat model alone captures most of the predictive signal, with clinical and peritumoral features providing only modest incremental value. The performance of all models across classifiers is summarized in eTable 3. Calibration curves (Fig. 3E–H) showed good agreement between predicted and observed outcomes across all cohorts, with HL test P values of 0.345 (training), 0.183 (validation), 0.561 (external test 1), and 0.300 (external test 2), confirming the reliability of the combined model.

A, B, C, and D show the AUC values in the training, validation, external test sets1, and external test sets2. E, F, G, and H show the calibration curves of the training, validation, external test sets1, and external test sets2, demonstrating that the model is accurate, efficient, and stable.

Nomogram for clinical decision support

A nomogram incorporating clinical stage, MRI tumor diameter, Peri3mm Rad-score, and Habitat Rad-score was constructed for individualized LNM risk assessment (Fig. 4). The Youden index in the training cohort (0.734) yielded an optimal cutoff of 0.32 (85 total points), with a sensitivity of 0.857 and specificity of 0.877 (eTable 2). Applied without recalibration to validation cohorts, this cutoff maintained consistent discrimination (sensitivity: 0.818–0.913; specificity: 0.732–0.877; eTable 2). Patients with total points ≥ 85 (probability ≥ 0.32) may be considered for upfront definitive chemoradiotherapy, whereas those with < 85 could be candidates for radical hysterectomy. When para-aortic LNM is suspected on imaging, extended-field radiotherapy or surgical staging is advised regardless of the nomogram score.

Furthermore, Decision curve analysis confirmed net clinical benefit of the combined model across a range of threshold probabilities (eFigure 8).

The nomogram incorporates clinical stage, MRI tumor diameter, Peri3mm radiomics score, and Habitat radiomics score. The optimal threshold of 0.32 (≈ 85 total points) distinguishes high-risk from low-risk patients for treatment guidance.

Evaluation of consistency between imaging and pathological habitats

Among 12 tumor-bearing nude mice (4 per cell line), 66 image-pathology section pairs were visually matched. After Dice and IoU evaluation, 44 pairs met the registration criteria (Dice > 0.8, IoU > 0.7) and were selected for analysis (eTable 3). Imaging habitats (K-means, optimal k = 4 by elbow method) and pathological habitats (hierarchical clustering) were generated for these sections (Fig. 5B–C). Concordance between imaging and pathological habitats was assessed using ARI for spatial correspondence and ICC (area) for proportional consistency (Table 3). ARI values ranged from 0.4 to 0.6, indicating moderate spatial agreement, while ICC (area) ranged from 0.8 to 1.0, indicating high consistency in the relative proportions of different habitat categories.

Table 3
The consistency of imaging and pathological habitats

Slice	ARI	ICC	Slice	ARI	ICC	Slice	ARI	ICC
HeLa1-2	0.556	0.897	U14(1)-8	0.580	0.962	U14(4)-3	0.459	0.974
HeLa2-5	0.565	0.898	U14(2)-3	0.579	0.953	U14(4)-4	0.473	0.942
HeLa2-6	0.556	0.897	U14(2)-4	0.409	0.841	U14(4)-5	0.473	0.964
HeLa3-3	0.574	0.960	U14(2)-5	0.416	0.887	SiHa1-1	0.472	0.942
HeLa3-4	0.583	0.931	U14(2)-6	0.418	0.947	SiHa1-2	0.473	0.964
HeLa3-6	0.575	0.960	U14(2)-7	0.383	0.928	SiHa1-3	0.470	0.890
HeLa4-1	0.576	0.940	U14(2)-8	0.580	0.962	SiHa1-4	0.452	0.814
HeLa4-3	0.585	0.931	U14(3)-1	0.409	0.841	SiHa2-1	0.455	0.822
HeLa4-5	0.576	0.940	U14(3)-2	0.416	0.887	SiHa2-2	0.483	0.942
U14(1)-1	0.561	0.939	U14(3)-3	0.418	0.947	SiHa2-3	0.539	0.993
U14(1)-2	0.558	0.933	U14(3)-4	0.470	0.890	SiHa3-2	0.542	0.917
U14(1)-3	0.561	0.939	U14(3)-5	0.452	0.814	SiHa3-3	0.473	0.942
U14(1)-4	0.561	0.951	U14(3)-6	0.455	0.822	SiHa4-1	0.473	0.964
U14(1)-5	0.560	0.908	U14(3)-7	0.483	0.942	SiHa4-2	0.473	0.942
U14(1)-6	0.561	0.951	U14(4)-1	0.456	0.792			

Discussion

To our knowledge, this study is the first multicenter study to integrate intratumoral habitat imaging with peritumoral radiomics for predicting preoperative LNM in CC using only T2WI. The combined model showed favorable predictive performance, with AUCs of 0.858 and 0.863 in two external test cohorts. A nomogram with a cutoff of 0.32 (85 points) was constructed for risk stratification: patients with probability ≥ 0.32 may be considered for definitive chemoradiotherapy, while those below this threshold could be candidates for radical hysterectomy. This decision aid offers gynecologic and radiation oncologists a cost-effective and simple practical tool for appropriate treatment planning. Moreover, the biological relevance of habitat imaging was further explored using a CC mouse model with 3D-printed registration technology.

The performance of traditional radiomics in this study (AUC = 0.815) aligns with recent systematic review estimates (AUC = 0.85, 95% CI: 0.81–0.88)[18]. The habitat model achieved higher AUCs (0.896 in validation, 0.822–0.829 in external tests) outperforms traditional radiomics and demonstrated superior sensitivity and specificity for detecting LNM compared to PET-CT[19]. SHAP analysis revealed opposing roles of the three subregions: H2 features drove LNM-positive predictions, whereas H1 features contributed to excluding LNM. The top H2-derived feature (GLRLM Short Run Emphasis) has been linked to tumor invasiveness in prior studies[20, 21], while the top H1 feature (GLCM-Maximum Probability) has been associated with low recurrence risk[22, 23]. These findings support the biological relevance of habitat-derived features.

To directly validate the biological correspondence of imaging habitats, we performed spatial registration between T2WI unsupervised clusters and HE-stained pathological clustering in animal models using 3D-printed molds. ARI values (0.4–0.6) indicated moderate spatial agreement, reflecting inherent spatiotemporal heterogeneity and registration precision limits, while ICC (area) (0.8–1.0) indicated high consistency in the relative proportions of functional regions. These findings suggest that while pixel-level spatial alignment remains challenging, habitat imaging reliably captures the overall composition of pathological phenotypes, supporting its potential for noninvasive tumor characterization.

Recently, Wang et al.[24] also confirmed the value of MRI habitat analysis in predicting preoperative LNM in CC. However, their study integrated T2WI and DWI sequences to construct a model and included postoperative lymphovascular space invasion (LVSI) indicators, which further improved predictive performance (AUC = 0.895). Nevertheless, this study was a single-center, small-sample design, and LVSI is a postoperative pathological indicator, limiting the model's clinical generalizability and preoperative application. In contrast, our multicenter study using T2WI alone achieved comparable performance (AUC: 0.858–0.863 externally) with a more generalizable design. Additionally, we explored the association of inflammatory markers (PAR, PLR, and SII) with LNM. Although these indicators have been reported to be related to the prognosis of CC[17, 25], no independent association with LNM was found in this study, suggesting their predictive value requires further validation. Furthermore, this study found that a tumor diameter of ≥ 4cm and higher clinical staging are independent risk factors for LNM, consistent with the conclusions of Chen et al.[26]. Integrating clinical and imaging features modestly improved performance, supporting the value of multimodal information. The Youden index-derived cutoff (0.32) enhanced the clinical actionability of the nomogram. Moreover, incorporation of peritumoral radiomic features—particularly the 3 mm expansion—improved predictive performance compared with intratumoral features alone, consistent with prior studies[27–29]. This suggests that the peritumoral microenvironment harbors information relevant to LNM status, though the underlying mechanisms require further investigation.

This study has several limitations. First, and most importantly, the retrospective surgical cohort design introduces selection bias. All included patients underwent radical hysterectomy with lymphadenectomy to obtain pathological LNM status. Therefore, our proposed 0.32 cutoff for triaging patients to

chemoradiotherapy versus surgery remains hypothesis-generating and requires prospective validation in non-surgical populations. Until then, the nomogram should be used to supplement, not replace, clinical judgment. Second, LNM prediction was based on tumor-derived imaging phenotypes rather than direct segmentation of metastatic lymph nodes; future models incorporating both primary tumor and nodal information may further improve accuracy. Third, using T2WI alone, while enhancing clinical feasibility, limits the characterization of tumor biology compared with multiparametric MRI. The animal experiment, though supportive of imaging–pathology correspondence, used subcutaneous xenografts that do not model lymphatic metastasis. Future studies should explore multiparametric MRI-based models and validate them in prospective cohorts.

Conclusions

In conclusion, this multicenter study developed and externally validated a T2WI-based habitat nomogram for preoperative LNM prediction in CC. The model offers a cost-effective and interpretable tool for risk stratification, with biological plausibility supported by animal experiments. Prospective studies in non-surgical populations are warranted before clinical implementation.

Abbreviations

ARI
Adjusted Rand Index
AUC
area under the curve
CC
cervical cancer
CH
Calinski-Harabasz
DB
Davies-Bouldin
DCA
Decision curve analysis
GLCM
gray-level co-occurrence matrix
GLRLM
gray-level run-length matrix
GLSZM
gray-level size zone matrix
HL
Hosmer-Lemeshow
ICC
intraclass correlation coefficient
ICC(area)
Intraclass Correlation Coefficient of Area
LASSO
Absolute Shrinkage and Selection Operator
LNM
lymph node metastasis
mRMR
Minimum Redundancy Maximum Relevance
NGTDM
neighboring gray-tone difference matrix
PAR
platelet-to-albumin ratio
PLR
platelet-to-lymphocyte ratio
RF
Random Forest
SC
Silhouette Coefficient
SII
systemic immune-inflammation index
SVM
Support Vector Machine

Declarations

Ethics approval and consent to participate

The ethical committee of Xijing Hospital, Fourth Military Medical University evaluated and approved the research protocol (Approval Number: KY20232107-F-1; Approval Date: 2023-4-14) and granted an informed consent waiver. All animal experiments were approved by the Institutional Animal Ethics Committee of Fourth Military Medical University (Approval Number: 20250031), and were performed in accordance with the ARRIVE guidelines and the Guidelines for the Care and Use of Laboratory Animals. No animals were privately owned by another institution, individual, or farm; therefore, no owner consent was required. This study followed the guidelines of the Declaration of Helsinki and local regulations.

Consent for publication

Not applicable.

Competing interests

The authors declare that they have no competing interests.

Funding

This study was supported by the Science and Technology Plan Projects of Xi'an Municipal Bureau of Science and Technology, Shaanxi Province, China (program number: 24YXYJ0034). The funding was primarily used for data analysis.

Author Contribution

BC, XH, and JR conceptualized the study. YW, HL, XH, MZ, and YG curated the data. BC acquired the funding. SL and JL conducted the investigation. YL and YW developed the methodology and performed the software analysis. JL, JR administered and supervised the project. YL validated the results. YL, YW and HL wrote the original draft. BC, XH, and JR reviewed and edited the manuscript. All authors read and approved the final manuscript.

Acknowledgements

The authors are grateful to the onekey AI platform for their essential statistical assistance.

Data Availability

The datasets generated and analyzed during the current study are not publicly available due to patient privacy and institutional data protection policies but are available from the corresponding author on reasonable request.

References

1. Lee ST, Lee YL, Chung CH, Chien WC, Li ST, Yao CY, Tzeng NS. Cervical cancer and risk of dementia: real-world insights from a nationwide cohort study in Taiwan. Int J Gynecol Cancer. 2024;34(8):1156–64.
2. Bhatla N, Berek JS, Cuello Fredes M, Denny LA, Grenman S, Karunaratne K, Kehoe ST, Konishi I, Olawaiye AB, Prat J, et al. Revised FIGO staging for carcinoma of the cervix uteri. Int J Gynaecol Obstet. 2019;145(1):129–35.
3. Sung H, Ferlay J, Siegel RL, Laversanne M, Soerjomataram I, Jemal A, Bray F. Global Cancer Statistics 2020: GLOBOCAN Estimates of Incidence and Mortality Worldwide for 36 Cancers in 185 Countries. CA Cancer J Clin. 2021;71(3):209–49.
4. Zeinalkhani F, Kamali Hakim P, Aghasi M, Mahdavi Sabet F, Mortazavi Ardestani R, Baghban Y, Malek M, Zeinalkhani H, Delazar S, Shakki Katouli F, et al. Direct comparison of full protocol MRI and modified non-contrast MRI in staging of cervical cancer: a retrospective study. Abdom Radiol (New York). 2025;51(1):316–28.
5. Selman TJ, Mann C, Zamora J, Appleyard T-L, Khan K. Diagnostic accuracy of tests for lymph node status in primary cervical cancer: a systematic review and meta-analysis. CMAJ. 2008;178(7):855–62.
6. Dessources K, Aviki E, Leitao MM. Lower extremity lymphedema in patients with gynecologic malignancies. Int J Gynecol Cancer: Official J Int Gynecol Cancer Soc. 2020;30(2):252–60.
7. Song J, Hu Q, Ma Z, Zhao M, Chen T, Shi H. Feasibility of T(2)WI-MRI-based radiomics nomogram for predicting normal-sized pelvic lymph node metastasis in cervical cancer patients. Eur Radiol. 2021;31(9):6938–48.
8. Xiao M, Ma F, Li Y, Li Y, Li M, Zhang G, Qiang J. Multiparametric MRI-Based Radiomics Nomogram for Predicting Lymph Node Metastasis in Early-Stage Cervical Cancer. J Magn Reson Imaging: JMRI. 2020;52(3):885–96.
9. McGranahan N, Swanton C. Biological and therapeutic impact of intratumor heterogeneity in cancer evolution. Cancer Cell. 2015;27(1):15–26.
10. Kim M, Park JE, Kim HS, Kim N, Park SY, Kim Y-H, Kim JH. Spatiotemporal habitats from multiparametric physiologic MRI distinguish tumor progression from treatment-related change in post-treatment glioblastoma. Eur Radiol. 2021;31(8):6374–83.

11. Jardim-Perassi BV, Huang S, Dominguez-Viqueira W, Poleszczuk J, Budzevich MM, Abdalah MA, Pillai SR, Ruiz E, Bui MM, Zuccari DAPC, et al. Multiparametric MRI and Coregistered Histology Identify Tumor Habitats in Breast Cancer Mouse Models. Cancer Res. 2019;79(15):3952–64.
12. Huang Z, Huang W, Jiang L, Zheng Y, Pan Y, Yan C, Ye R, Weng S, Li Y. Decision Fusion Model for Predicting Microvascular Invasion in Hepatocellular Carcinoma Based on Multi-MR Habitat Imaging and Machine-Learning Classifiers. Acad Radiol. 2025;32(4):1971–80.
13. Zhang H, Zheng Y, Zhang M, Wang A, Song Y, Wang C, Yang G, Ma M, He M. Breast Cancer: Habitat imaging based on intravoxel incoherent motion for predicting pathologic complete response to neoadjuvant chemotherapy. Med Phys. 2025;52(6):3711–22.
14. Kanungo T, Mount DM, Netanyahu NS, Piatko CD, Silverman R, Wu AY. An efficient k-means clustering algorithm: analysis and implementation. IEEE Trans Pattern Anal Mach Intell. 2002;24(7):881–92.
15. Yan Y, Feng X, Luo X. Spatially aware adjusted Rand index for evaluating spatial transcriptomics clustering. Biometrics 2025, 81(3).
16. Liljequist D, Elfving B, Skavberg Roaldsen K. Intraclass correlation - A discussion and demonstration of basic features. PLoS ONE. 2019;14(7):e0219854.
17. Kozasa K, Mabuchi S, Komura N, Yokoi E, Hiromasa K, Sasano T, Kawano M, Matsumoto Y, Kobayashi E, Kimura T. Comparison of clinical utilities of the platelet count and platelet-lymphocyte ratio for predicting survival in patients with cervical cancer: a single institutional study and literature review. Oncotarget. 2017;8(33):55394–404.
18. Jiang CQ, Li XJ, Zhou ZY, Xin Q, Yu L. Imaging based artificial intelligence for predicting lymph node metastasis in cervical cancer patients: a systematic review and meta-analysis. Front Oncol. 2025;15:1532698.
19. He T, Sun J, Wu J, Wang H, Liang C, Wang H, Li S, Su S. PET-CT versus MRI in the diagnosis of lymph node metastasis of cervical cancer: A meta-analysis. Microsc Res Tech. 2022;85(5):1791–8.
20. Park H, Kim KA, Jung J-H, Rhie J, Choi SY. MRI features and texture analysis for the early prediction of therapeutic response to neoadjuvant chemoradiotherapy and tumor recurrence of locally advanced rectal cancer. Eur Radiol. 2020;30(8):4201–11.
21. Yu H, Meng X, Chen H, Liu J, Gao W, Du L, Chen Y, Wang Y, Liu X, Liu B, et al. Predicting the Level of Tumor-Infiltrating Lymphocytes in Patients With Breast Cancer: Usefulness of Mammographic Radiomics Features. Front Oncol. 2021;11:628577.
22. Vamvakas A, Williams SC, Theodorou K, Kapsalaki E, Fountas K, Kappas C, Vassiou K, Tsougos I. Imaging biomarker analysis of advanced multiparametric MRI for glioma grading. Phys Med. 2019;60:188–98.
23. Hashimoto K, Haraguchi T, Nawata S, Wada S, Hamaguchi S, Nishio M, Mimura H. Creation of a Prediction Model of Local Tumor Recurrence After a Successful Conventional Transcatheter Arterial Chemoembolization Using Cone-Beam Computed Tomography Based-Radiomics. Cardiovasc Intervent Radiol. 2024;47(11):1495–505.
24. Wang M, Cao Y, Zhang W, Liang Y, Liu J, Lei J. Prediction Model of Lymph Node Metastasis in Cervical Cancer Based on MRI Habitat Radiomics. Cancers (Basel) 2025, 18(1).
25. Staniewska E, Grudzien K, Stankiewicz M, Raczek-Zwierzycka K, Rembak-Szynkiewicz J, Nowicka Z, Tarnawski R, Miszczyk M. The Prognostic Value of the Systemic Immune-Inflammation Index (SII) and Red Cell Distribution Width (RDW) in Patients with Cervical Cancer Treated Using Radiotherapy. Cancers 2024, 16(8).
26. Chen X-L, Chen G-W, Xu G-H, Ren J, Li Z-L, Pu H, Li H. Tumor Size at Magnetic Resonance Imaging Association With Lymph Node Metastasis and Lymphovascular Space Invasion in Resectable Cervical Cancer: A Multicenter Evaluation of Surgical Specimens. Int J Gynecol Cancer: Official J Int Gynecol Cancer Soc. 2018;28(8):1545–52.
27. Zhang Z, Wan X, Lei X, Wu Y, Zhang J, Ai Y, Yu B, Liu X, Jin J, Xie C, et al. Intra- and peri-tumoral MRI radiomics features for preoperative lymph node metastasis prediction in early-stage cervical cancer. Insights Imaging. 2023;14(1):65.
28. Xu H, Wang A, Zhang C, Ren J, Zhou P, Liu J. Intra- and peritumoral MRI radiomics assisted in predicting radiochemotherapy response in metastatic cervical lymph nodes of nasopharyngeal cancer. BMC Med Imaging 2023, 23(1).
29. Wang Z, Zhang H, Lin F, Zhang R, Ma H, Shi Y, Yang P, Zhang K, Zhao F, Mao N, et al. Intra- and Peritumoral Radiomics of Contrast-Enhanced Mammography Predicts Axillary Lymph Node Metastasis in Patients With Breast Cancer: A Multicenter Study. Acad Radiol. 2023;30(Suppl 2):S133–42.

Figures

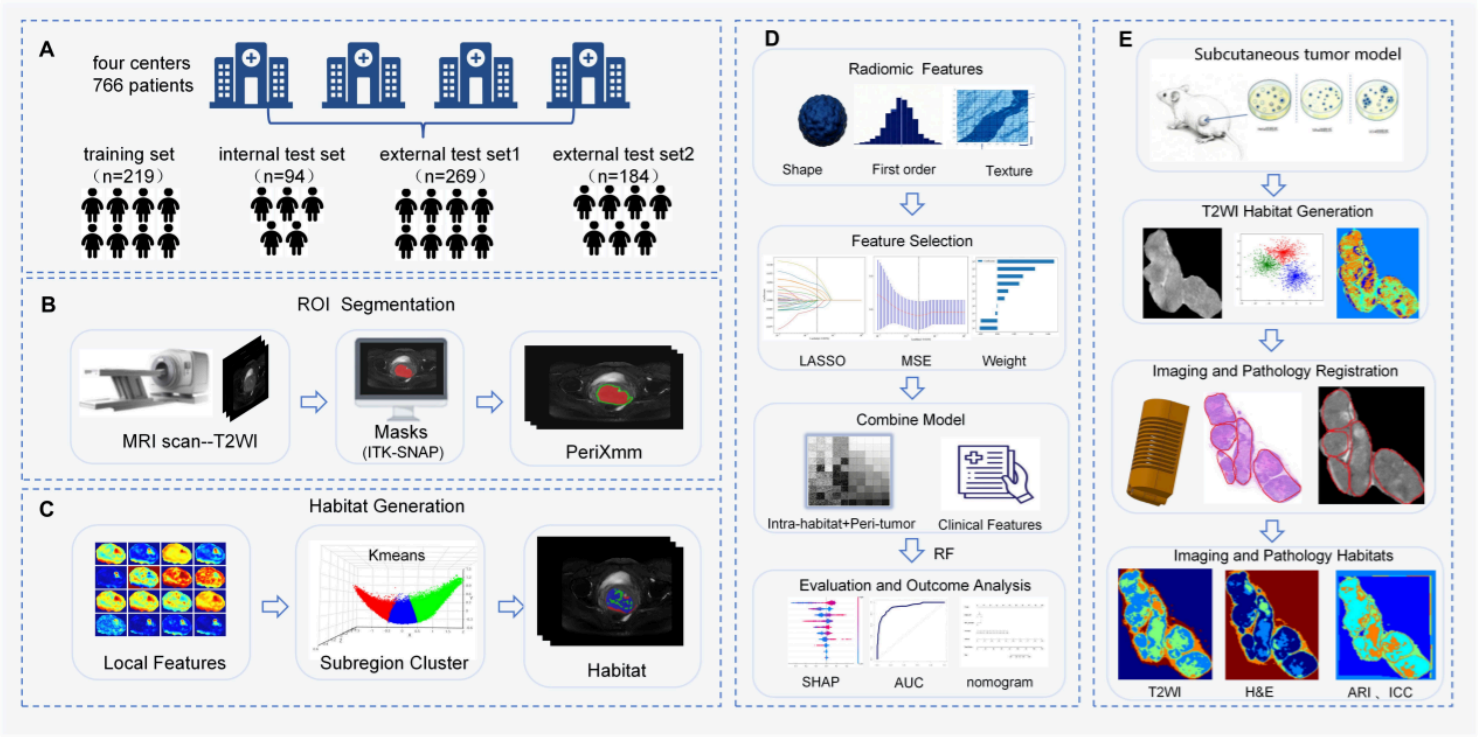


Figure 1

The overall workflow of the study

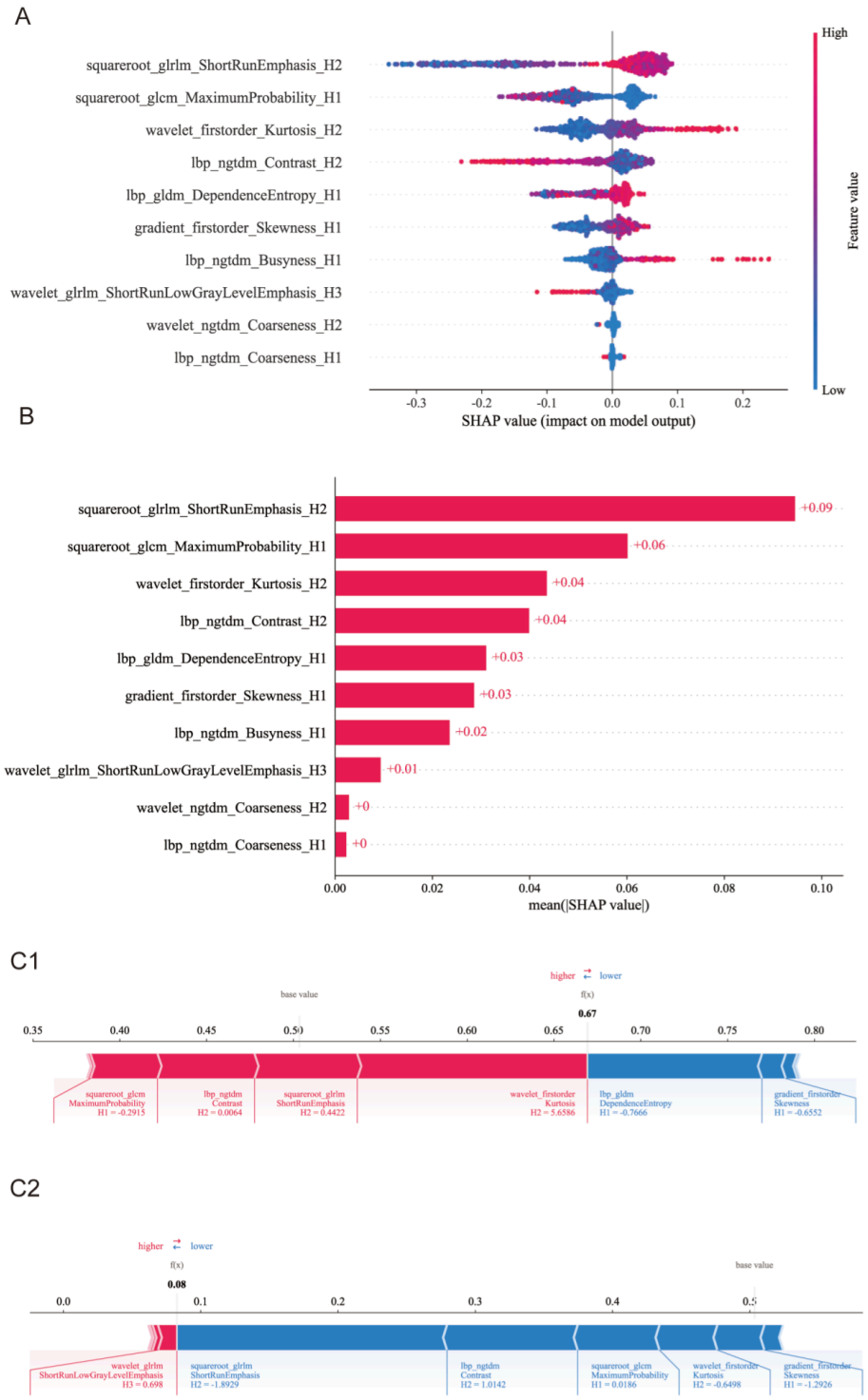


Figure 2

The SHAP analysis of the Habitat Signature model

A: Distribution of SHAP values across habitat-derived features for all samples, highlighting their relative contribution to LNM prediction. B: The features are ranked according to their mean absolute SHAP values to identify the most influential predictors in the model. C: It provides patient-level interpretability through two representative cases: C1 illustrates a patient with LNM, where positive SHAP contributions from key features shift the prediction of metastasis, whereas C2 depicts a patient without LNM, in which negative SHAP contributions suppress the likelihood of metastasis.

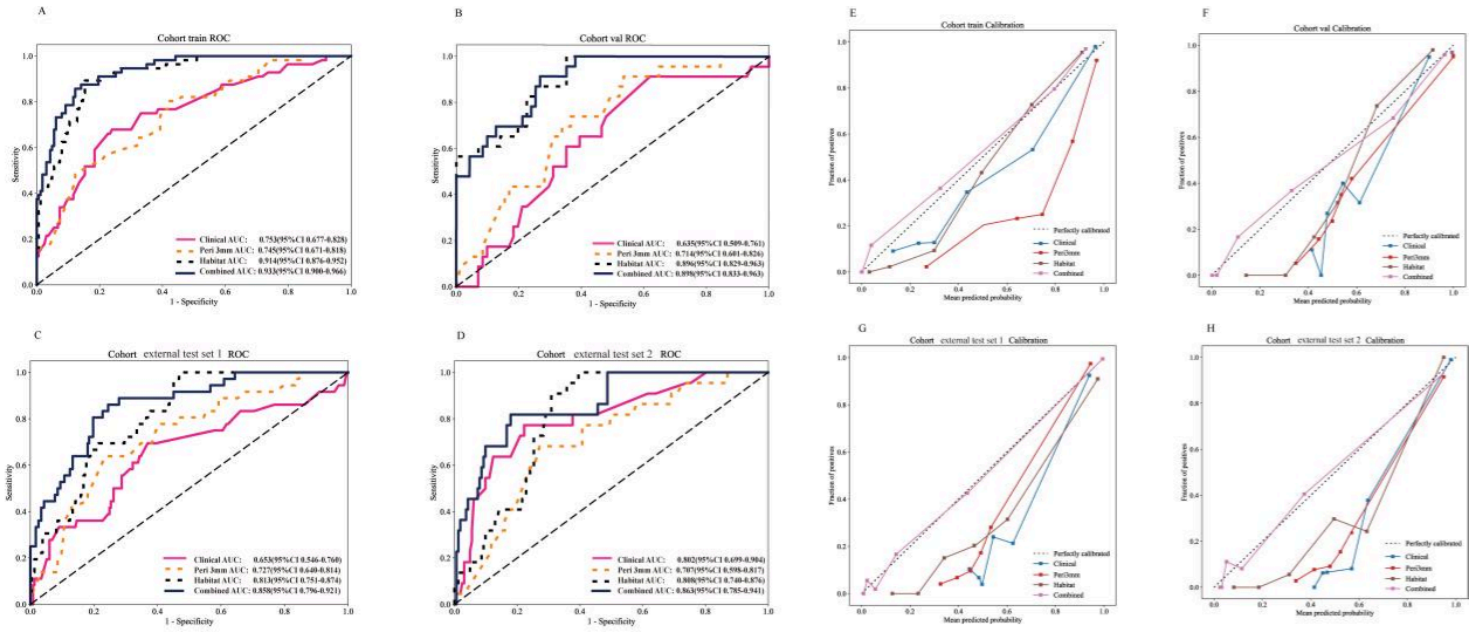


Figure 3

The AUC values and calibration curve of all signatures across four cohorts.

A, B, C, and D show the AUC values in the training, validation, external test sets1, and external test sets2. E, F, G, and H show the calibration curves of the training, validation, external test sets1, and external test sets2, demonstrating that the model is accurate, efficient, and stable.

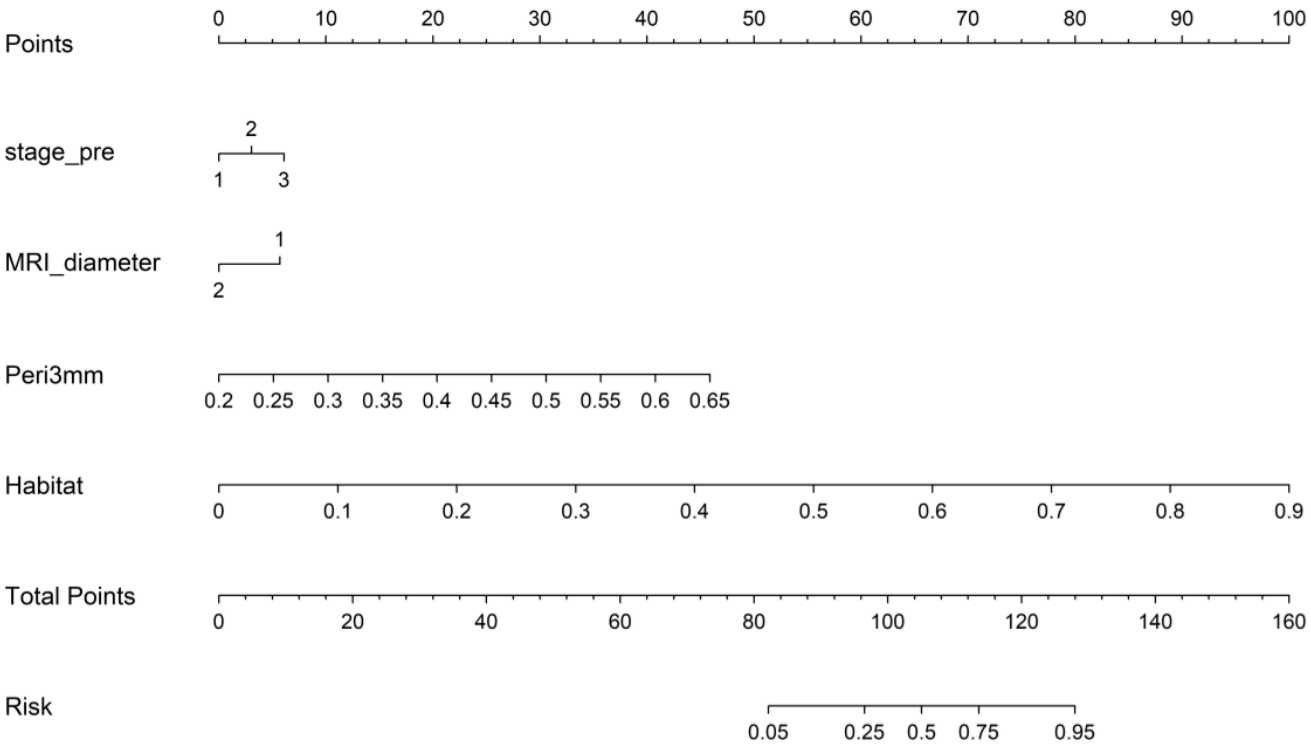


Figure 4

Nomogram for individualized preoperative LNM risk prediction in cervical cancer.

The nomogram incorporates clinical stage, MRI tumor diameter, Peri3mm radiomics score, and Habitat radiomics score. The optimal threshold of 0.32 (≈85 total points) distinguishes high-risk from low-risk patients for treatment guidance.

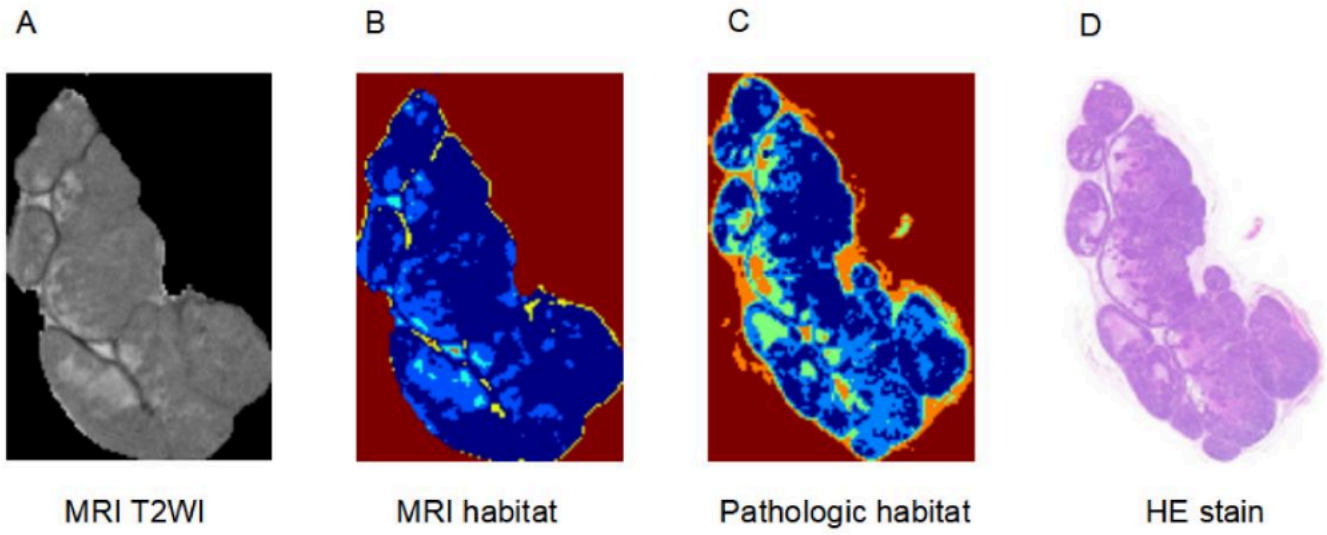


Figure 5

Examples of Imaging and Pathological Habitat Clustering

Supplementary Files

This is a list of supplementary files associated with this preprint. Click to download.

- Supplementarymaterials.docx